

*1N 93-CR
092 289*

FINAL REPORT - D.O. 163

NAS8-38609

**COSMIC RAY ENERGY DETERMINATION BY THE
REDUCED-OPENING ANGLE METHOD**

**Cosmic Ray Laboratory
College of Science
The University of Alabama in Huntsville
Huntsville, AL 35899**

**Prepared by:
Dr. Arthur E. Smith**

**Principal Investigator:
Dr. John C. Gregory**

February 1998

Summary

- The reduced opening angle technique offers a simple way with minimal model dependence to measure cosmic ray energies over a broad range without any normalization uncertainties.
- The emulsion film and CR39 detectors proposed are well established techniques and should perform adequately.
- The analysis method depends on accurate automatic scanning of the CR39 plates. UAH have developed such a capability.
- With the proposed geometry energy measurements to ~ 5 TeV/a can be made.
- The expected iron event rate ($E \geq 500$ GeV/a) is $10 \text{ m}^{-2} \text{ day}^{-1}$.
- The expected energy resolution, from accelerator calibrations at 200 GeV/a, is -50% to +80%. Since the absolute flux has some sensitivity to the assumed power law index it is essential that good energy resolution is obtained.
- The expected charge resolution is ~ 0.3 charge units for the CNO group falling to ~ 1 charge unit for the iron group.
- A suitable event trigger would be a measurable ($\geq 2 \text{ } \mu\text{m}$) deflected heavy ($Z > 2$) fragment.
- One potential background is electromagnetic dissociation that predominantly couples to individual protons or alphas. Although the cross-sections can be appreciable such events will not pass the event trigger.

1. INTRODUCTION:	5
2. THE REDUCED OPENING ANGLE TECHNIQUE	5
2.1 The physics of the technique	5
2.2 The formalism	6
2.3 Comparison with experimental heavy-ion beam data.	7
2.4 Experimental data	8
3. THE PROPOSED DETECTOR	10
4. THE EXPECTED PERFORMANCE	11
4.1 The fragment distribution.	11
4.2 The Charge resolution	14
4.3 The energy resolution and the maximum energies that can be measured.	14
4.4 Event rates.	14
4.5 Determination of the absolute intensity of the primary cosmic radiation.	15
4.5.1 The detection efficiency	15
4.5.2 Fragmentation processes in the overlying atmosphere.	16
4.5.3 The effects of energy resolution and the geomagnetic cutoff momentum.	16
5. CONCLUSIONS	17
6. APPENDICES	17
6.1 Appendix A: Electromagnetic dissociation	17
6.2 Appendix B: Nuclear cross-sections and their energy dependence ($E < 10.6 \text{ GeV/a}$).	19
6.3 Appendix C: Some measured fragment distributions	20

Figure 1 q^2 distribution of α -fragments for various projectile at several energies.....7
 Figure 2 Accelerator calibrations of the opening angle technique.....9
 Figure 3 q^2 distribution for α fragments from a range of cosmic ray primary particles.....9
 Figure 4 q^2 distribution for a range of incident cosmic rays where the emission angle has
 been scaled according to equation 5.10
 Figure 5 Schematic diagram of the proposed detector construction.....11
 Figure 11 Target factors for a 10.6 GeV/a ^{197}Au on three targets.18

Figure 8 The yield of all fragments with $Z \geq 2$ as a function of fragment number for a
 ^{197}Au projectile.22
 Figure 9 The ratio of the protons yield to the number of events as a function of the
 number of released protons for a ^{197}Au projectile.22
 Figure 10 Pseudo rapidity distributions for a ^{197}Au projectile.22

Table 1 Values of the electron scattering radii and associated parameters.....11
 Table 2 Parameters for equation 15.12
 Table 3 Calculated cross-sections for a 500 GeV/a iron cosmic ray incident on a lead
 target. No nuclear structure effects are included. The cross-sections should be taken
 only as a semi-quantitative guide.....13
 Table 4 The deflections in μm at a distance of 0.3 m for a range of species and for γ values
 between 500 and 5000 (0.499-4.999 TeV/a).....14
 Table 5 The aperture factor for two 1 m^2 detectors as a function of their separation.15
 Table 6 The expected iron event rate for two 1 m^2 detectors separated by 0.3 m.....15
 Table 7 Measured electromagnetic dissociation cross-sections for ^{197}Au projectiles and
 deduced values for iron (see text).19
 Table 8 Fit parameters for hard sphere models with overlap terms given by equations 25
 and 26.20
 Table 9 Iron and lead cross-sections calculated with and without energy dependent
 models.20

1. Introduction:

Accurate measurement of the primary galactic cosmic ray species energy dependence in the regime beyond ~ 500 GeV/a is difficult due to the low flux and the limitations of energy measurement techniques. However, such observations are essential to resolve several questions of current interest such as: Is the enrichment of heavy species ($Z \geq 6$) cosmic rays first reported at higher energies by the proton satelliteⁱ and then later at lower energiesⁱⁱ real? The results from a previous deployment of the reduced opening angle technique are inconclusive^{vi} but the authors do point to limitations in the previous techniques. Another intriguing puzzle is the energy dependence of silicon cosmic rays. Two independent experiments using different experimental techniques indicate that silicon is under-abundant. At present the observation is limited by statistics; it could still be a three sigma fluctuation. However, if confirmed the current models of acceleration and propagation which are species independent are seriously inadequate.

To progress further the species and energy dependence must be accurately measured in a manner that is free from systematic uncertainty. In this report we show that the reduced opening angle method offers a simple and relatively inexpensive method to answer these questions.

First we present the physics of the reduced opening angle and indicate the expected energy and charge resolution. The proposed detector design is then presented followed by the expected performance. Where ever possible simple phenomenological expressions that allow 'back of the envelope' estimates are given. More details are presented in the appendices. The limit of the energy resolution and the expected event rates for iron cosmic rays are calculated. Salient points are summarized in the conclusions.

2. The reduced opening angle technique

2.1 The physics of the technique

The method relies on the experimental observation that the fragments from an high energy collision, in the rest-frame of the projectile, have a universal isotropic Gaussian momentum distribution that is independent of the fragment mass: the decay is independent of formation^{iii,iv}. The target nucleus acts only to inject energy into the projectile, raising it to a state of high excitation and causing it to 'explode' into a number of fragments. There is no memory of how the energy was transferred. The relative probability for a given fragment is independent of the excitation process. We note in passing that this technique shares most features of the Castagnoli^v method² used for mesons.

² The Castagnoli method is derived from the well known relation $\tan\theta \cong \gamma_L \tan\theta^*/2$ between the lab. angle θ and the c.m. angle θ^* . This is obtained by the approximation that $\epsilon^* = \sqrt{p^{*2} + m^2} \sim p^*$ in the c.m.s. This approximation is not applicable in the case of evaporated fragments from nuclei since $p^* \sim p_F \ll M_N$. Hence $\epsilon^* \sim M_N$.

2.2 The formalism

We shall closely follow the formalism of Ichimura et al^{vi}. We first restrict the discussion to α -particles and then show how this may be extended.

With the α opening angle technique the primary energy per nucleon (E_0) is given by:

$$E_0 \approx P_0 \approx \frac{P_{T\alpha}}{\sin \theta_\alpha} \approx \frac{\langle P_{T\alpha} \rangle}{\theta_\alpha} \quad 1.$$

with $\langle P_{T\alpha} \rangle \approx 70-90$ MeV/c, where θ_α is the emission angle of the α in the laboratory system. Though equation (1) is easy to use, the energy being determined from the quotient of $\langle P_{T\alpha} \rangle$ to θ_α , there are several practical problems:

- 1) Fluctuation from the mean
- 2) The energy is influenced strongly by the most forward α -particle
- 3) Not all the fragments are α -particles.

The third problem is most critical especially for light nuclei: oxygen to silicon. A solution to these difficulties has been developed based on the theoretical model of Goldhaber^v. Let P_f be the total momentum of a fragment with mass number A_f produced from the projectile with mass number A_p . Goldhaber showed that the mean square momentum $\langle P_f^2 \rangle$ in the projectile rest frame is given by:

$$\langle P_f^2 \rangle = \langle P_N^2 \rangle \frac{A_f (A_p - A_f)}{A_p - 1} \quad 2.$$

where $\langle P_N^2 \rangle$ is the mean square momentum of a nucleon. It is approximately relatedⁱⁱⁱ to the Fermi momentum p_f by

$$\sqrt{\langle P_N^2 \rangle} = \sqrt{\frac{3}{5}} p_f \approx 180 \text{ MeV} / C \quad 3.$$

Although equation 2 is derived from simple assumptions it reproduces heavy-ion-beam fragment data well^{vii}. Using this equation we immediately obtain the following relation

$$\langle P_{Tf}^2 \rangle = \langle P_{TN}^2 \rangle \frac{A_f (A_p - A_f)}{(A_p - 1)} \quad 4.$$

with $\langle P_{TN}^2 \rangle = (2/3) \langle P_N^2 \rangle$; the transverse momentum is expressed per nucleon.

We have so far only considered α -particles. To extend the model to the full range of fragment species we introduce a reduced angle θ given by:

$$\theta = \theta_f \sqrt{\frac{A_f(A_p - 1)}{(A_p - A_f)}}$$

5.

The reduced angle calculated from equation 5 is independent of the mass of both the projectile and the fragment. Hence while the angular distribution ϕ depends on the projectile energy as well as the participant masses by using the reduced angle a considerable simplification occurs:

$$\phi(E_0, \theta_f; A_f, A_p) d\theta_f^2 = \phi(q) dq^2$$

6.

with $q \equiv \beta_L \gamma_L \theta \approx \gamma_L \theta$, where β_L and γ_L are the velocity ($c = 1$) of the projectile in the lab. system and its Lorentz factor.

This is a crucial result: we can treat equivalently any fragment p , α , Li, Be, ... Consequently the fluctuations in the average transverse momentum will be considerable reduced from those that come with only measuring individual α -particles.

2.3 Comparison with experimental heavy-ion beam data.

The validity of the scaling law (equation 6) can be seen in Fig. 1. The scaling law holds for a range of species over a wide energy range. The shape may be reproduced by the summation of two Gaussian curves fit to the experimental data with the constraint that $\tau_1 + \tau_2 = 1$.

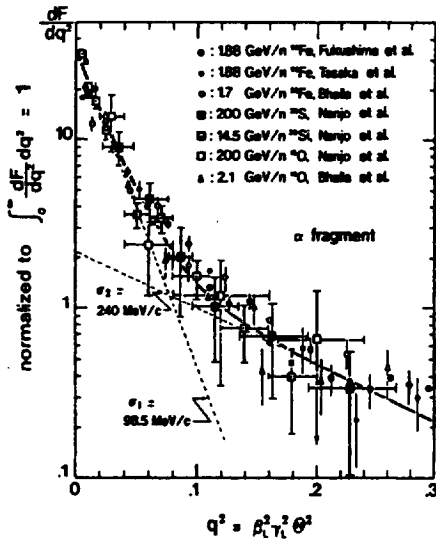


Figure 1 q^2 distribution of α -fragments for various projectile at several energies.

$$\phi = \tau_1 a_1^2 e^{(-a_1^2 q^2)} + \tau_2 a_2^2 e^{(-a_2^2 q^2)}$$

7.

with $a_{1,2} = \frac{M_N}{\sqrt{2}\sigma_{1,2}}$, $\tau_1=0.7252$, $\tau_2=0.2748$, $\sigma_1 = 98.5$ MeV/c, $\sigma_2 = 239.6$ MeV/c.

8.

We now calculate the mean value of $\ln q$ ($= \ln \beta_L \gamma_L \theta$)

$$\langle q \rangle = \int_0^\infty \ln q \phi(q) dq^2 = -\frac{1}{2} \gamma + \ln \frac{\sqrt{2\sigma_0}}{M_N}$$

9.

where γ ($=0.5772$) is the Euler constant, and

$$\sigma_0 = \sigma_1^{\tau_1} \sigma_2^{\tau_2} = 125.8 \text{ MeV} / c$$

so that

$$\gamma_L = \sqrt{1 + \gamma_0^2 e^{-2\langle \ln \theta \rangle}} \approx \gamma_0 e^{-\langle \ln \theta \rangle}$$

10.

Hence the average value of θ is given by

$$\langle \theta \rangle = \frac{\gamma_0}{\gamma_L}$$

11.

with

$$\gamma_0 = \frac{\sqrt{2\sigma_0}}{M_N} e^{-\gamma/2} = 0.1422$$

12.

The mean value of $\langle \ln \theta \rangle$ is obtained experimentally by

$$\langle \ln \theta \rangle = \frac{1}{n_f} \sum_{i=1}^{n_f} \ln \theta_i$$

13.

where n_f is the number of fragments.

From a practical point it is important to to exclude wounded protons (protons that receive significantly more energy transfer) and or π^{\pm} 's in the measured data. To reduce their number minimum ionizing events with emission angles five times the smallest are excluded in addition to a cut made on the charge sum restriction.

2.4 Experimental data

This applicability of this technique has been studied using accelerator beams and works well as shown in Figure 2.

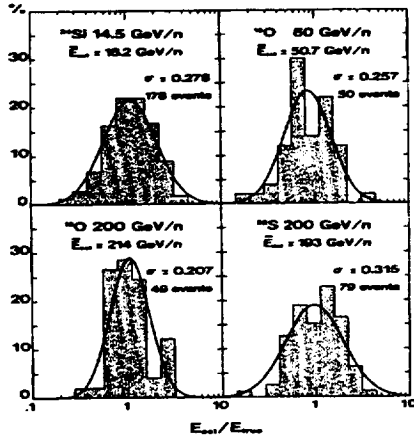
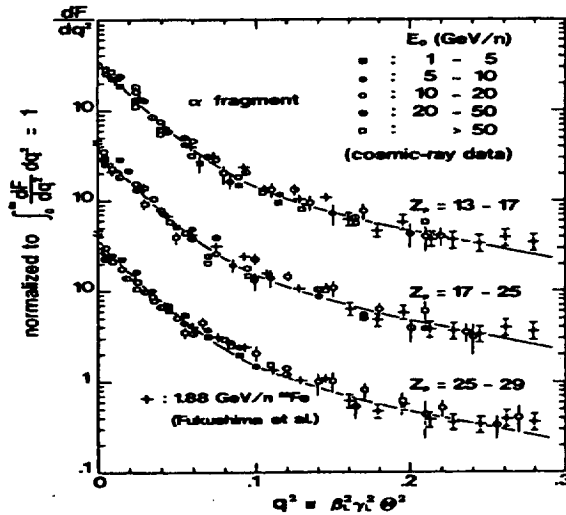


FIG. 7. Resolution of our energy determination calibrated by heavy-ion beams at several energies.

Figure 2 Accelerator calibrations of the opening angle technique.

The standard deviation σ is of magnitude 0.2 - 0.3 for $\log_{10} E_{est}/E_{true}$. Taking a putative σ of 0.25 the 200 GeV/a data lies between 112.3 and 356 GeV/a. That is a one sigma error of -44% to +78%.



The q^2 distributions for α events from a range of incident cosmic ray projectiles is shown in Figure 3. There is a remarkable species and energy independence to the distribution.

Figure 3 q^2 distribution for α fragments from a range of cosmic ray primary particles.

For the present purposes we are also interested in the q^2 distribution for heavy fragments which is shown in Figure 4. The angle scaling works remarkably well clearly demonstrating that the technique can be used for all fragment species so long as the fragment mass is known.

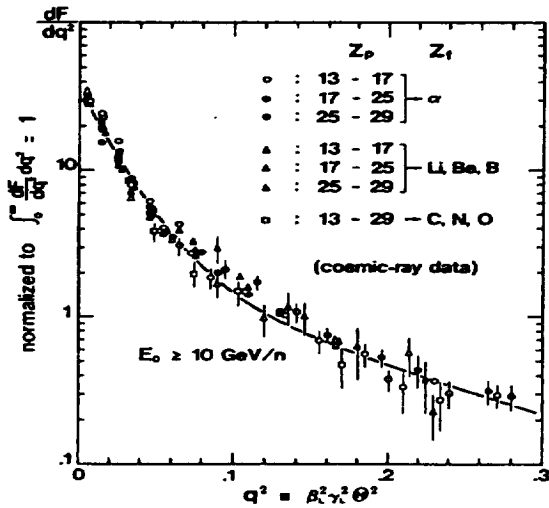
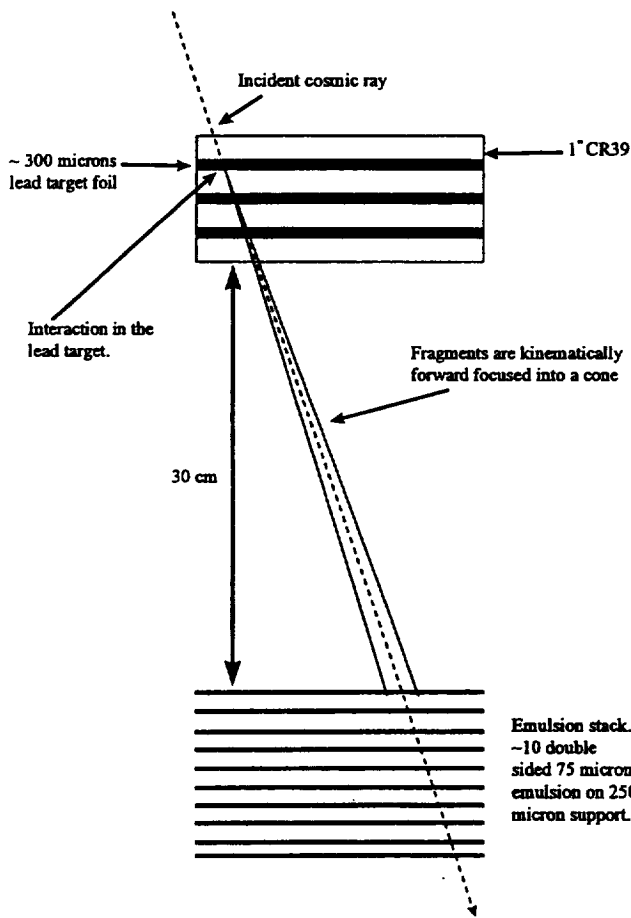


Figure 4 q^2 distribution for a range of incident cosmic rays where the emission angle has been scaled according to equation 5.

3. The Proposed detector



The proposed detector is relatively simple. It would consist of a number of modules as shown schematically in Figure 5. To reduce development and fabrication times and to minimize the instrument cost each module would be the same size (40x50 cm) as used for JACEE experiments.

UAH has developed digital tracking techniques so that the cosmic ray species and the trajectory can be determined automatically by scanning the CR39 plates. Using this information the expected location of the pool of fragments on the emulsion is examined and the fragment charge and angular deviation determined. Hence, as discussed in 2.2, the energy of the cosmic ray can be determined.

Figure 5 Schematic diagram of the proposed detector construction

For the design proposed here lead target foils are suggested. However it would also be possible to use silver emulsions as a target. This was the approach adopted by Ichimura^{vi} et al.

4. The expected performance

4.1 The fragment distribution.

Nuclear interaction fragment cross-sections have been measured at energies up to 10.6 GeV/a for ultra heavy nuclei by Garrard et al.^{viii} and Waddington et al.^{ix}. A detailed discussion of the total and partial charge changing cross-sections is presented by Nilsen et al.^x. Since the total charge changing cross-section provides an upper bound to the measurements and since new values based on nuclear charge radii are presented by Nilsen et al. We will first discuss them.

The conventional^{xi} approach to nuclear cross-section calculation has been to take the radius^{xi} as a constant $\times A^{1/3}$. There are several problems with this approach. Firstly hydrogen does not naturally fit into the series and more importantly electron scattering form factors indicate that nuclear charge radii do not scale directly as $A^{1/3}$. As many charge radii have been measured a more useful approach is to use these data (Nilsen et al.^x.) In Table 1 we show some measured radii taken from their paper.

	H	Li	C	Al	Fe	Cu	Kr
$r_0=R_c^3/A^{1/3}$ fm	1.034	1.64	1.36	1.25	1.27	1.28	1.22
$R_w^4=1.35A^{1/3}$ fm	1.35	2.57	3.09	4.05	5.16	5.39	5.91
R_c fm	1.034	3.13	3.11	3.75	4.85	5.11	5.34
$R_n^5 = SR_c$	1.32	4.00	3.97	4.79	6.19	6.52	6.82
	Ag	Sn	Xe	La	Ho	Au	Pb
$r_0=R_c/A^{1/3}$ fm	1.23	1.20	1.21	1.21	1.22	1.17	1.19
$R_w=1.35A^{1/3}$ fm	6.45	6.63	6.86	6.99	7.40	7.85	7.99
R_c fm	5.87	5.90	6.15	6.27	6.69	6.81	7.04
$R_n = SR_c$	7.39	7.53	7.85	8.01	8.54	8.70	8.99

Table 1 Values of the electron scattering radii and associated parameters.

Nilsen find the best fit to the energy-independent charge changing cross-sections⁶ is

$$\sigma(R_p, R_T) = \pi \times \left[R_p + R_T - (3.20 \pm 0.05) \right]^2$$

³ R_c is the measured electron scattering radius.

⁴ R_w is a conventional radius using a normalization of $1.35 \times A^{1/3}$ as used by Westfall.

⁵ R_n is the nuclear radius computed as a scaling factor (1.277) times the charge radius.

⁶ Cross-sections are usually measured in barns (10^{-28}m^2) whereas nuclear radii are measured in fermi (10^{-15}m). Hence 1 barn = 100 fm^2 .

14.

The radii used are the matter radii (R_m) taken from Table 1. For iron cosmic rays hitting a lead target we expect a total charge changing cross-section of 4509 mb. Nilsen et al. have extended their model to incorporate logarithmic energy dependence. However, the relatively small energy change from 0.6 GeV/a to 10.6 GeV/a produces a set of very different parameters see appendix B. Moreover, Nilsen et al. express reservations (see their paper for an explicit discussion) about extrapolating these expressions to higher energies. Hence we will use equation 14 to calculate our reference cross-section.

Estimation of the partial cross-sections is more difficult. Some authors^{xii>xiii} believe that at high energies in the regime beyond reaction thresholds and resonance's the cross-sections will have only a small logarithmic energy dependence. Here we will present some estimates based on Nilsen et al. The models are relatively crude containing no nuclear structure information and are unlikely to give a good description of data at the high energies which are of primary interest in this report. However, they do provide some guidance. Measured fragment yields for 10.6 GeV/a gold projectiles are presented in appendix C. These demonstrate the limitations of these simple models.

We compute the partial charge changing cross-section according to the prescription presented by Nilsen et al. Here ΔZ is the change in the projectile charge. It can be positive (a pickup-reaction) although it is predominantly negative (a stripping reaction):

$$\sigma_{\Delta Z}(A_p, A_T, K, \Delta Z) = p_1(A_p^{1/3} + A_T^{1/3} - p_2)\left(1 + \frac{P_3}{K}\right)|\Delta Z|^{-p_4[1 + A_p^{1/3}/P_5 + A_T^{1/3}/P_6 + P_7/K]}$$

15.

The parameters are given in Table 2. $A_{p,T}$ are the projectile and target masses respectively and K is the kinetic energy (Total energy - m_0c^2) in GeV/a.

P_1	21.2±0.5 mb
P_2	1.08±0.15
P_3	(0.485±0.014)A GeV
P_4	0.094±0.013
P_5	1.11±0.02
P_6	10.8±1.6
P_7	(0.85±0.03)A GeV

Table 2 Parameters for equation 15.

Nilsen et al. also presents simple phenomenological algorithms, with a simple energy scaling, to calculate the expected fragment distribution yield. No nuclear structure information is included and the modeled energy dependence gives asymptotic energy independence in the regime of interest here. We also note the cross-section algorithms were optimized for the fragmentation of ultra heavy nuclei where one would expect some

washing out of the strong structural effects seen in sd shell ($Z= 8$ to 20). Although the cross-sections were derived from relatively low energy (≤ 10.6 GeV/a) data it is anticipated that there will be no serious deviation from the weak energy dependence incorporated in the model. However, it should be borne in mind that older attempts to extrapolate nuclear cross-sections at lower energies have frequently been found inadequate when higher energy data became available. The cross-sections are shown in Table 3.

Cosmic ray energy		Total cross-section ⁷		Total charge changing cross-section ⁸	
500 GeV/a		4508 mb		1869 mb	
Z_change	Cross-section (mb)	% of the charge changing cross-section ⁹	Z_change	Cross-section (mb)	% of the charge changing cross-section
+1	184	9.8	-13	55	3.0
-1	184	9.8	-14	53	2.9
-2	133	7.1	-15	51	2.8
-3	109	5.9	-16	50	2.7
-4	96	5.1	-17	49	2.6
-5	86	4.6	-18	47	2.5
-6	79	4.2	-19	46	2.5
-7	74	4.0	-20	45	2.4
-8	69	3.7	-21	44	2.4
-9	66	3.5	-22	43	2.3
-10	62	3.3	-23	42	2.3
-11	60	3.2	-24	42	2.2
-12	57	3.1	-25	41	2.2

Table 3 Calculated cross-sections for a 500 GeV/a iron cosmic ray incident on a lead target. No nuclear structure effects are included. The cross-sections should be taken only as a semi-quantitative guide.

⁷ The total cross-section calculated from equation 14.

⁸ The charge changing cross-section calculated from equation 15.

⁹ These are % of the total charge-changing cross-section. (equation 15) which has been greatly extrapolated from its know region of validity. NB Since the total hadronic cross-section is calculated from equation 14 to be twice that of equation 15 these values are uncertain to at least a factor of 2.

4.2 The Charge resolution

The charge resolution is determined by the CR 39 etch detectors. Typical values of ≤ 0.3 charge units should be achieved for CNO group cosmic rays falling to ~ 1 for iron group species.

4.3 The energy resolution and the maximum energies that can be measured.

The measured energy resolution (one sigma) for projectile energies up to 200 GeV/a is -44% to +78% as shown in section 2.4.

For a practical detector the limiting energy resolution is set by the smallest deflection that can be measured which is itself controlled by the physical separation between the target and emulsion plates (see Figure 5). For comparison purposes we will take the following practical conditions:

- 1) Target to emulsion separation 0.3 m
- 2) Emulsion grain sizes of 0.1 μm and the minimum deflection that can be measured is 2 μm .

Using equation 11 we calculate the average emission angle and relate this angle to a specific fragment angle using equation 5. In Table 4 we show the calculated deflections in μm as a function of energy. If we set our detection criterion as at least one heavy ($Z > 2$) fragment we can perhaps hope to measure energies to ~ 5 TeV/a with this geometry.

γ	H	^4He	^9Be	^{12}C	^{16}O	^{20}Ne	^{24}Mg	^{28}Si	^{32}S	^{36}Ar	^{40}Ca
500	85.3	41.5	26.3	22.0	18.2	15.4	13.3	11.5	10.0	8.6	7.3
1000	42.7	20.7	13.2	11.0	9.10	7.72	6.64	5.75	4.98	4.29	3.6
1500	28.4	13.8	8.8	7.3	6.1	5.1	4.4	3.8	3.3	2.9	2.4
2000	21.3	10.4	6.6	5.5	4.6	3.9	3.3	2.9	2.5	2.1	1.8
2500	17.1	8.3	5.3	4.4	3.6	3.1	2.7	2.3	2.0	1.7	1.5
3000	14.2	6.9	4.4	3.7	3.0	2.6	2.2	1.9	1.7	1.43	1.2
3500	12.2	5.9	3.8	3.2	2.6	2.2	1.9	1.6	1.4	1.2	1.0
4000	10.7	5.2	3.3	2.8	2.3	1.9	1.7	1.4	1.3	1.1	0.9
4500	9.5	4.6	2.9	2.5	2.0	1.7	1.5	1.3	1.1	1.0	0.8
5000	8.5	4.2	2.6	2.2	1.8	1.5	1.3	1.2	1.0	0.9	0.7

Table 4 The deflections in μm at a distance of 0.3 m for a range of species and for γ values between 500 and 5000 (0.499-4.999 TeV/a).

4.4 Event rates.

The instrument has been modeled as two parallel rectangles placed directly above one another and separated by a constant distance. The aperture factor has been computed¹⁰ using the techniques of Sullivan^{xiv} for arbitrary dimensions. However no attempt has been made to allow for the finite detector thickness nor for nuclear interaction

¹⁰ Code is on Smiles in the directory \$2\$dka100:[smitha.nuc_int]ap_fac_rectangle.for

losses. Hence the numbers are upper limits. A flight instrument would probably use JACEE geometry (40×50 cm) but for comparison purposes we here present the aperture factors for two square (1 m²) detectors.

Sheet separation (cm)	Aperture factor (m ² sr)
20	2.17
30	1.82
40	1.54
50	1.30
100	0.63

Table 5 The aperture factor for two 1 m² detectors as a function of their separation.

To calculate the event rate we will take aperture factor for a sheet separation of 30 cm, an exposure of 1 day, and calculate¹¹ the integral iron event rate for a range of energies.

γ	TeV/a	Iron event rate/day with 0.3m between two square (1 m ²) detectors.
100	0.1	111
500	0.5	10
1000	1.0	4
5000	5.0	0.3
10,000	10.0	0.1
50,000	50.0	0.009
100,000	100.0	0.004

Table 6 The expected iron event rate for two 1m² detectors separated by 0.3 m.

4.5 Determination of the absolute intensity of the primary cosmic radiation.

The determination of the absolute intensity of the primary cosmic radiation depends on a knowledge of three factors (that will be discussed separately):

1. The detection efficiency
2. The fragmentation in the overlying air mass
3. The effects of the energy resolution and the geomagnetic cutoff momentum.

4.5.1 The detection efficiency

Often it is difficult to calculate the detection efficiency for a counter experiment. One of the advantages of the reduced opening angle technique is the simple geometry.

¹¹ Code is on Smiles in the directory \$2\$dka100:[smitha.bugs.flux]int_flg_rec

Hence the predominant uncertainty is the nuclear cross-section. There are several models including the one we discuss in appendix B that uses measured nuclear charge radii rather than values scaled by the cube root of the average element mass. Ichimura et al.^v used such a simple scaling model of Karol^{xv} and found that this did give a good reproduction of the measured cross sections as determined from the ratio of jets to primary particles. Hence the uncertainties introduced by the cross-section calculations are relatively small.

4.5.2 Fragmentation processes in the overlying atmosphere.

By necessity any balloon deployment will be below an overlying atmosphere of 5-10 g/cm². Since this is the common situation a number of techniques have been developed to correct a measured flux to that at the top of the atmosphere. The techniques must also account for the flux of secondary particles (from the interaction of primaries with the atmosphere) and correct the measured flux accordingly. There are a number of reviews in the literature including that employed by Ichimura et al.^{vi} in their deployment of the reduced opening angle technique. Uncertainties from such atmospheric interactions are small and quantifiable.

4.5.3 The effects of energy resolution and the geomagnetic cutoff momentum.

The factor required to calculate the measured flux from the observed flux depends on the geomagnetic cutoff momentum, the energy resolution and the power law index of the incoming cosmic radiation. Below ~ 20 GeV/a a simulation was used by Ichimura et al.^{vi} to compute the effect of the geomagnetic cutoff. Beyond ~ 20 GeV/a the predominant effect of decreasing energy resolution is to require a larger correction. There is still some sensitivity to the power index as shown: This is undesirable and is best controlled by making good measurements so that the energy resolution is small. The variation with the assumed power index of the primary radiation is relatively small if the value of $\log_{10}(E_{\text{est}}/E_{\text{true}})$ is in the range of 0.2 to 0.3 as was obtained by Ichimura et al.^{vi} in their accelerator measurements. For similar cosmic ray species the relative flux ratios will be well determined but should the energy resolution change significantly with species both the relative and absolute intensities may not be reliable.

5. Conclusions

The reduced opening angle technique offers a simple way to measure the charge and energy of cosmic rays. The technique has minimal model dependence at least up to several hundred GeV/a. As all the measurements would be made with the same optical techniques there are no energy normalization uncertainties.

The energy range that can be addressed is limited by the instrument dimensions. The instrument can in principle be scaled to dimensions limited only by the lifting vehicle. In practice the needs for accurate geometric reference points is also a demanding constraint. For the geometry suggested here (flight path of 30 cm) energy measurements to ~ 5 TeV/a can be made with a charge resolution of ~ 0.3 for the CNO group to ~ 1 for the iron group. Energy resolutions of -50% to $+80\%$ have been obtained in accelerator calibrations at 200 GeV/a. A practical limit to the utility of the technique is set by the cosmic ray flux. The event rate per m^2 of the detector for iron cosmic rays exceeding 10 TeV/a is 0.1 per day.

The absolute flux measurements have a sensitivity to the assumed power index. The sensitivity is minimized if good energy resolution ($\log_{10}(E_{\text{est}}/E_{\text{true}}) \sim 0.2$) is obtained.

6. Appendices

6.1 Appendix A: Electromagnetic dissociation

Electromagnetic dissociation (EMD) occurs when the Lorentz contracted electric field of the target nucleus contributes to the fragmentation of the projectile nucleus. In a simple picture EMD occurs when a virtual photon is exchanged between the target nucleus and the projectile often resulting in the excitation of a giant multipole

resonance^{xvi}. The total cross-sections from electromagnetic processes can exceed the nuclear component but the charge changing electromagnetic cross-sections at least for gold projectiles are not large as measured by Geer et al.^{xvii}. The EMD component to such processes can be determined by the method of factorization where it has been shown that the partial $\sigma_{AZ}(T,F)$ for a given projectile can be separated into factors γ^F depending only on the fragment and γT depending only on the target.

$$\sigma_{AZ}(T, F) = \gamma^F \gamma T + \sigma_{EMD}(T, F) \quad 16.$$

where $\sigma_{EMD}(T,F)$ represents the EMD contribution. For this analysis the hydrogen partial cross-sections are used to define γ^F with $\gamma T=H=1$. Hydrogen σ are used since they should have minimal EMD. The other target σ are divided by the hydrogen σ to give.

$$\sigma_{AZ}(T, F) = \gamma T + \frac{\sigma_{EMD}(T, F)}{\gamma^F} \quad 17.$$

To determine the magnitude of γT a simple expression based on a fit to the cross-section is used.

$$\gamma T = \sqrt{\frac{\sigma(T)}{\sigma_0}} \quad 18.$$

where σ_0 (=2524 mb) is a normalization factor. Hence the EMD component can be determined by subtracting equation 17 from the total cross-section. Although no EMD cross-sections for iron are reported by Geer et al.^{xviii} we may estimate their magnitude as

$$\sigma_{EMD}(Fe) = \frac{26^2}{79^2} \times \sigma_{EMD}(Au) \quad 19.$$

Target	Measured $\Delta Z = -1$ σ (mb) for ^{197}Au projectiles on a range of targets	Measured $\Delta Z = -2$ σ (mb) for ^{197}Au projectiles on a range of targets	Deduced $\Delta Z = -1$ σ (mb) for ^{56}Fe projectiles on a range of targets	Deduced $\Delta Z = -2$ σ (mb) for ^{56}Fe projectiles on a range of targets
C	15±10	5±5	1.65	.55
Al	27±9	11±5	3.07	1.21
Cu	55±10	13±6	6.05	1.43
Sn	116±12	23±7	12.76	2.53
Pb	268±15	42±7	29.48	4.62

Table 7 Measured electromagnetic dissociation cross-sections for ^{197}Au projectiles and deduced values for iron (see text).

From comparing Table 3 and Table 7 it is clear that the EMD contribution to the total charge changing cross-section is $\sim 10\%$ for $\Delta Z = 1$ and less for larger charge changes. For the opening angle technique the reaction channels with only one proton out produce essentially no deviation in the cosmic ray trajectory and no energy determination can be made. Hence we can neglect the EMD component to the reaction channels for this technique.

6.2 Appendix B: Nuclear cross-sections and their energy dependence ($E < 10.6 \text{ GeV/a}$).

In this appendix we discuss the energy dependence of the measured nuclear cross-sections and present some simple phenomenological models that have been fit to data. Nilsen et al.^x have used a logarithmic scaling that was inspired by the logarithmic scaling used by the Particle Data Group^{xviii} at high energies to describe nucleon/nucleon interactions. They parameterize the cross-sections as:

$$\sigma(R_p, R_T) = \pi F(E) [R_p + R_T - G(E)\Delta R]^2 \quad 20.$$

$$F(E) = 1 + F_1 \text{Ln}(E) + F_2 [\text{Ln}(E)]^2 \quad 21.$$

$$G(E) = 1 + G_1 \text{Ln}(E) + G_2 [\text{Ln}(E)]^2 \quad 22.$$

The F value scales the entire expression whilst the G value modifies the overlap term ΔR . Both terms depend on energy and on the model used for the overlap term ΔR . Two variants for ΔR are considered by Nilsen et al: equations 23 and 24. Fits are provided for each term and a series of measured conditions as shown in Table 8. These fits include data from Nilsen et al. (a) and from Binns et al.^{xx} (b) and Geer et al.^{xx} (c)

$$\Delta R = r_0 \delta \quad 23.$$

$$\Delta R = \frac{r_0 \delta}{(A_P^{1/3} + A_T^{1/3})}$$

24.

Equation	F ₁	F ₂	G ₁	G ₂	N _v ²
25 ¹²	-1.512±0.012	1.11±0.04	-1.41±0.04	0.96±0.06	4.65
25 ¹³	-1.61±0.16	1.18±0.14	-1.51±0.19	1.04±0.18	3.92
25 ¹⁴	-0.28±0.10	0.09±0.03	-0.40±0.10	0.11±0.04	4.88
26 ¹²	-1.24±0.19	0.95±0.16	-1.6±0.3	1.1±0.2	4.73
26 ¹³	-1.28±0.18	0.98±0.14	-1.6±0.3	1.1±0.2	4.07
26 ¹⁴	-0.23±0.07	0.09±0.02	-0.60±0.11	0.21±0.04	4.86

Table 8 Fit parameters for hard sphere models with overlap terms given by equations 23 and 24.

The computed cross-sections have a strong energy dependence as shown in Table 9. The necessity to use only the parameter specially developed for the particular energy regime of interest is clear.

Equation	Parameters	Energy	σ barns
	None	All	4.509
22	25 ¹³	1.5 GeV/a	4.69
22	25 ¹³	10.6 GeV/a	6.115
22	26 ¹⁴	10.6 GeV/a	2.701

Table 9 Calculated cross-sections for iron projectiles on lead targets. Models with and with out energy dependence have been used – see text for details.

6.3 Appendix C: Some measured fragment distributions

In section 4.1 we present simple phenomenological formula for calculating nuclear fragment cross-sections. For the purposes of this study what may be of more interest are actual fragment yield data as presented by Waddington et al.^{xxi}. Although these have been measured at low energies and are for ultra heavy nuclei the distributions are of interest. However, any conclusions drawn from them are subject to these caveats.

In Figure 8 we show that the fragment yield ($Z \geq 3$) has little energy variation between 1 and 10.6 GeV/a.

¹² There are 43 values of Kr and Ag $\sigma(P,T,K)$ used in these fits from Nilsen et al's. paper.

¹³ These fits include the ten additional values of $\sigma(P,T,K)$ from Binns et al.

¹⁴ These fits include the six additional values at 10.6 GeV/a from Geer et al. with the electromagnetic contribution removed.

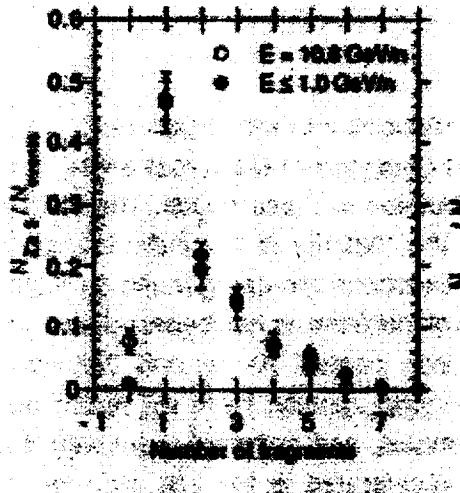


Figure 8 Comparison of the yield of $Z \geq 3$ fragments at 1 and 10.6 GeV/a with a ^{197}Au projectile.

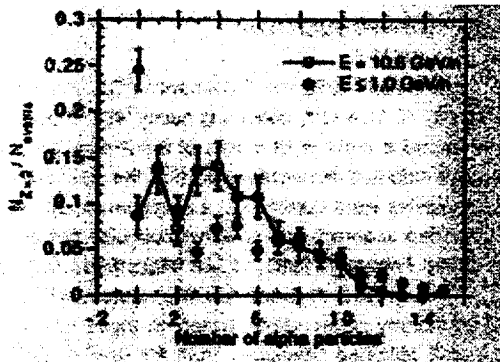


Figure 9 The fraction of α -particles to the total number of events at 1 and 10.6 GeV/a with a ^{197}Au projectile.

In contrast to Figure 8 the yield of α -particles show some energy dependence. As the energy increases fewer events have no α -particles and there is a distinct increase in the region of 3-5 α -particles. The number of fragments plus α 's (Figure 10) shows a strong move towards less fragments as the energy increases and the yield of protons also increases with energy (Figure 11).

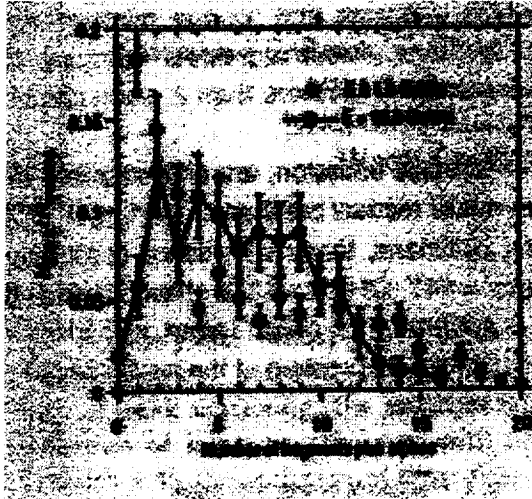


Figure 10 The yield of all fragments with $Z \geq 2$ as a function of fragment number for a ^{197}Au projectile.

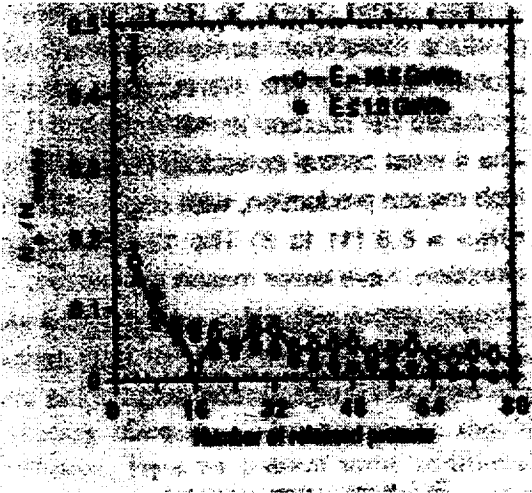
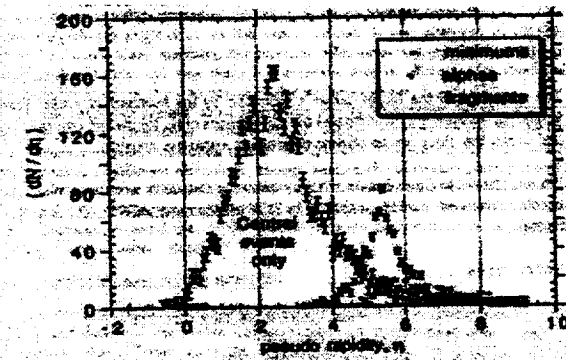


Figure 11 The ratio of the protons yield to the number of events as a function of the number of released protons for a ^{197}Au projectile.



It is also interesting to look at the pseudo rapidity $(-\log_e[\tan\theta/2])$ distributions which are shown in Figure 12.

Figure 12 Pseudo rapidity distributions for a ^{197}Au projectile.

Although the minimum ionizing particles (protons and pions) peak at pseudo rapidity's of ~ 2.5 while the heavier fragments are at ~ 5.5 the tail of the minimum ionizing particles overlaps the $Z \geq 2$ particles. Hence it is essential that the

emulsion films employed be able to unambiguously identify protons and pions from all other species. This is also a requirement to guard against wounded protons contaminating the distribution – see section 2.2

ⁱ N.L. Grigorov, I.D. Rapport, I.A. Savenko, V.E. Nesterov, and V.L. Prokhim, in Proceedings of the 12th International Cosmic Ray Conference, Hobart, Tasmania, 1971, Conference Papers, edited by A.G. Fenton and K.B. Fenton (University of Tasmania Press, Hobart, Tasmania, 1971), Vol. 5, pp. 1746, 1752 and 1760.

ⁱⁱ See e.g. and references therein E. D. Olson, *Results from an Antarctic Balloon Flight* Proceedings of the 24th ICRC, Rome Italy Vol, 2, OG.1 - OG. 6 752 (1995).

ⁱⁱⁱ H. Feshbach, K. Huang Phys. Lett 47B (1973) 300

^{iv} A.S. Goldhaber Phys. Lett 53B (1974) 306

^v C. Castagnoli et al., Nuovo Cimento 10, 1261 (1953)

^{vi} M. Ichimura, et al. “Observations of heavy cosmic-ray primaries over the wide energy range from ~ 100 GeV/particle to ~ 100 TeV/particle: Is the celebrated “knee” actually so prominent?” Phys Rev D 48 (1993) 1949

^{vii} J. Huffner, Phys. Rep. 85 (1985) 129

^{viii} T.L. Garrard, J.R. Cummings, L.Y. Geer, J.Klarmann, B.S. Nilsen and C.J. Waddington. “Nuclear Interaction Cross Sections for UltraHeavy Nuclei” 24th International Cosmic Ray conference, Rome, 1995, OG 8.2.7 192.

^{ix} C.J. Waddington et al. “Fragmentation of High Energy UH nuclei’ 23rd ICRC, Calgary, OG 8.0.11 (1993) 203.

^x B.S. Nilsen, C.J. Waddington, J.R. Cummings, T.L. Garrard, and J. Klarmann. “Fragmentation cross sections of relativistic $^{84}_{36}\text{Kr}$ and $^{109}_{47}\text{Ag}$ nuclei in targets from hydrogen to lead.” Phys. Rev. C 52, 3277 (1995)

^{xi} G.D. Westfall, L.W. Wilson, P.J. Lindstorm, H.J. Crawford, D.E. Greiner, and H.H. Heckman, Phys. Rev. C 19, 1309 (1979)

^{xii} J. Benecke, T.T. Chou, C.N. Uang, and E.Yen, Phys. Rev. 188, 2159 (1969)

^{xiii} H. Boggild and T. Ferbel, Annu. Rev. Nucl. Sci. 24, 451 (1974)

^{xiv} J.D. Sullivan “Geometric factor and directional response of single and multi-element particle telescopes” NIM, 95 (1971) 5

^{xv} P.J. Karol, Phys Rev. C **22**, 1203 (1975).

^{xvi} J.C. Hill, F.K. Wohn, D.D. Schwellenbach, Phys. Lett **B273**, 371 (1991)

^{xvii} L.Y. Geer, J. Klarmann, B.S. Nilsen, C.J. Waddington, W.R. Binns, J.R. Cummings and T.L. Garrard "Charge-changing fragmentation of 10.6 GeV/nucleon ¹⁹⁷Au nuclei" Phys. Rev. C **52** (1995) 334.

^{xviii} J. Benecke, T.T. Chou, C.N. Uang, and E. Yen, Phys. Rev. **188**, 2159 (1969).

^{xix} W.R. Binns, T. L. Garrard, M.H. Israel, M. P. Kertmann, J. Klarmann, E.C. Stone, and C.J. Waddington, Phys Rev. C **36**, 1870 (1987).

^{xx} L.Y. Geer, J. Klarmann, B.S. Nilsen, C. J. Waddington, W. R. Binns, J.R. Cummings, and T. L. Garrard, Phys. Rev C **51**, 334 (1995); L.Y. Geer, Ph.D. thesis, Washington University, 1995.

^{xxi} C.J. Waddington, M.L. Cherry, A. Dabrowska, P. Deines-Jones, A. I. Dubinina, O.K. Egorov, R. Holyński, W.V. Jones, A. Jurak, E.D. Kolganova, E.A. Pozharova, K. Sengupta, T. Yu. Skorodko, V.A. Smirnitski, M. Szarska, J.P. Wefel, B. Wilczynska and W. Wolter. "Fragmentation of High Energy UH Nuclei" Proceedings of the 23 ICRC Calgary, OG 6-10 203 (1993)